

ENABLING NONLINEAR MANIFOLD PROJECTION REDUCED-ORDER MODELS BY EXTENDING CONVOLUTIONAL NEURAL NETWORKS TO UNSTRUCTURED DATA*

JOHN TENCER[†] AND KEVIN POTTER[†]

Abstract. We propose a nonlinear manifold learning technique based on deep autoencoders that is appropriate for model order reduction of physical systems in complex geometries. Convolutional neural networks have proven to be highly advantageous for systems demonstrating a slow-decaying Kolmogorov n -width. However, these networks are restricted to data on structured meshes. Unstructured meshes are often required for performing analyses of real systems with complex geometry. Our custom graph convolution operators based on the available differential operators for a given spatial discretization effectively extend the application space of these deep autoencoders to systems with arbitrarily complex geometry that can only be efficiently discretized using unstructured meshes. We propose sets of convolution operators based on the spatial derivative operators for the underlying spatial discretization, making the method particularly well suited to data arising from the solution of partial differential equations. We demonstrate the method using examples from heat transfer and fluid mechanics and show better than an order of magnitude improvement in accuracy over linear subspace methods.

Key words. manifold learning, model order reduction, convolutional neural network, autoencoder

AMS subject classifications. 35Q35, 35Q68, 35Q74, 35Q79,

1. Introduction. The simulation of parameterized dynamical systems is common across a wide range of application spaces. In many of these applications, the effort is motivated by solving a set of partial differential equations (PDEs), whose accurate solution often requires a fine spatial resolution that creates a large state-space dimension for the resulting system of ordinary differential equations (ODEs). As a result, numerical integration of the resulting system of ODEs is computationally costly and, in some circumstances, (such as many-query or time-critical problems) this is infeasible.

Projection based reduced-order models (ROMs) offer an accurate alternative to the direct numerical integration of these systems of ODEs for a substantially lowered computational cost, but only when a low-dimensional trial subspace can be identified[31, 2]. Projection-based ROMs involve two stages: (1) a computationally expensive offline stage that involves computing state snapshots at different times for samples of the parameter space and using those snapshots to define a low-dimensional trial subspace, and (2) a computationally inexpensive online stage, computing approximate trajectories restricted to lie within the trial subspace.

The vast majority of ROM development has focused on the use of linear trial subspaces selected via balanced truncation [21, 42, 25, 3], rational interpolation [1, 13], or proper orthogonal decomposition (POD) [7, 65, 2, 6, 9, 20]. These types of projection methods can be expected to be very accurate with a very low-dimensional trial subspace for problems that exhibit fast decaying Kolmogorov n -width. However, many problems (particularly advection-dominated problems) exhibit slowly decaying Kolmogorov n -width requiring a larger trial subspace dimension to achieve accurate results. High-dimensional trial subspaces are undesirable as the dimension of the

*Submitted to the editors June 8, 2020.

Funding: This work was funded by the Laboratory Directed Research and Development program at Sandia National Laboratories

[†]Sandia National Laboratories, Albuquerque, NM (jtencer@sandia.gov, kmpotte@sandia.gov).

trial subspace is directly related to the online computational cost of the ROM.

For problems with slow-decaying Kolmogorov n -widths, nonlinear trial subspaces (defined via deep autoencoders [51]) can theoretically reduce computational costs while maintaining accuracy [38, 17]. However, the most common type of deep autoencoder, fully-connected networks, are infeasible for large-scale systems with large state spaces. Convolutional neural networks (CNNs) are a highly advantageous architecture for this type of nonlinear manifold learning because the number of learnable weights in the network is independent of the input feature size (full-order model state space dimension), significantly reducing the computational cost [37]. CNNs are a powerful tool that has seen success in performing varied machine learning tasks, such as image classification [35, 63, 60, 57, 18, 36, 34, 53, 40], image super resolution [11, 54, 32, 30, 68, 49], natural language processing [29, 55, 12, 27, 56], and even physics [10, 61, 15, 62, 71, 69, 22, 8, 38, 39, 48, 19, 45]. Unfortunately, deep autoencoders are not currently widely applicable for model-order reduction of real-world applications, because convolutional networks are restricted to structured meshes (such as a sequence, 2D array of pixels, or 3D array of voxels). The requirement of a structured mesh makes it impossible to apply CNNs to problems with arbitrarily complex geometry, such as any real engineered system, without resorting to either resampling [45] or employing overset [58, 47, 41] or immersed boundary [50, 43] methods.

More recently, graph convolutional networks (GCNs) [67, 70] have been developed to deal with data on unstructured graphs such as those arising from wide-ranging application domains, including social networks [66], knowledge graphs [26], and computer vision [5]. The unstructured meshes commonly used for spatial discretization of complex systems are a subset of these general unstructured graphs. The analysis of data arising from computer simulation of physics problems is distinct from most types of learning tasks typically associated with GCNs. GCNs are typically designed to capture combinatorial structures like node degrees (the number of graph edges connected to a given node) that are irrelevant to the solution of PDEs [64]. Reliance on this connectivity information has caused issues in applications like computer vision where this structural information is irrelevant to the learning task [70]. Unlike the computer vision application, which is almost exclusively focused on triangle surface meshes (for which the most important attribute is the shape), nodal coordinates are also of little interest when attempting to reconstruct PDE solutions. In order to reproduce the solution manifold of a set of PDEs, the spatial distribution of the field discretized by the mesh (temperature, velocity, stress, etc.) is of primary concern.

In order to apply projection-based ROMs to the analysis of real engineered systems whose governing equations (advection-diffusion, Navier Stokes, Euler, etc.) preclude the existence of a sufficiently small linear trial subspace, a manifold learning method must be employed that is (1) practical for large state space dimensionality, (2) able to learn complex nonlinear embeddings, and (3) not restricted to structured meshes. Linear subspace methods satisfy 1 and 3 but not 2. Fully-connected autoencoder networks satisfy 2 and 3 but not 1. Traditional convolutional autoencoder networks satisfy 1 and 2 but not 3. In this work, we propose an extension of traditional convolution networks that is suited for data on unstructured meshes with arbitrary connectivity allowing the technique to be used for any discretized system. Our proposed manifold learning method is capable of satisfying all 3 requirements and is thus well suited to addressing this challenging analysis problem. We draw inspiration from prior work in the fields of graph neural networks and geometric learning and formulate a solution for our learning task that is customized to the learning of PDE solutions while fitting within the more general established framework of GCNs. Addi-

tionally, we seek implementations that are applicable to generic spatial discretizations, including mesh-free methods. As such, we use operators that involve discretization-independent learned weights. We propose sets of convolution operators based on the spatial derivative operators for the underlying spatial discretization, making the method particularly well-suited to data arising from the solution of PDEs. In the 3 exemplar problems chosen, our approach is consistently more than an order of magnitude more accurate than an optimal linear subspace method for low-dimensional trial subspaces.

The paper is organized as follows. Our new algorithm is described in [section 2](#) in the context of GCNs, the implementation details are given in [section 3](#) and [section 4](#), the numerical experiments corresponding results are described in [section 5](#). The conclusions follow in [section 6](#).

2. Graph Convolutions. There are two main types of GCNs, spectral and spatial. Spectral GCNs interpret the graph convolution operation as the application of a filter from the perspective of graph signal processing [59]. In contrast, spatial GCNs interpret the convolution operation through the lens of information propagation. The spatial approach can enable greater parallelism due to the inherently local nature of the operation. Although our contribution may be viewed through either lense, we derive our contribution as an extension to spectral GCNs and a special case of MoNet [44] due to the convenience of matrix notation afforded to spectral GCNs.

In the literature on GCNs, a graph is represented by $\mathcal{G} = (\mathcal{V}, \mathcal{E})$ where \mathcal{V} denotes the nodeset and $|\mathcal{V}| = n$ and \mathcal{E} denotes the edgeset. We use $v_i \in \mathcal{V}$ to denote a node and $e_{ij} = (v_i, v_j) \in \mathcal{E}$ denote an edge connecting v_i and v_j . We also have a node feature matrix $X \in \mathbb{R}^{n \times c}$ defining the c attributes present for each node.

We define the adjacency matrix $A \in \mathbb{R}^{n \times n}$, such that $A_{ij} = 1$ if $e_{ij} \in \mathcal{E}$ and $A_{ij} = 0$ if $e_{ij} \notin \mathcal{E}$. For stability reasons, it is customary to explicitly include self-loops in A , i.e. $A_{ii} = 1$. The adjacency matrix is normalized using the degree matrix $D \in \mathbb{R}^{n \times n}$, which is a diagonal matrix with $D_{ii} = \sum_j A_{ij}$. For GCNs, the graph Laplacian is defined as

$$(2.1) \quad L = D^{-1/2} A D^{-1/2},$$

and the graph convolution layer is then

$$(2.2) \quad X^{(l+1)} = \epsilon(LX^l W),$$

where ϵ is a nonlinear activation function and $W \in \mathbb{R}^{c_l \times c_{l+1}}$ is a trainable weight matrix.

We observe that the graph Laplacian is insufficiently expressive on its own owing to the comparatively small number of attributes per node for most common PDEs relative to what is typical in, for example social science [24, 33] or knowledge graphs [23]. Additionally, the graph Laplacian has the undesirable property of directly depending upon the local mesh connectivity in a way that may prevent it from being discretization-independent.

Equation (2.2) can be split up into 3 parts, a filter application or mixing step, a 1D convolution, and the application of the nonlinear activation function. The mixing step, which "mixes" information from a node's neighborhood, is the multiplication of L by the input feature matrix X^l . We generalize this mixing step by allowing for an arbitrary number of mixing operations, the results of which are concatenated along the feature/channel dimension:

$$(2.3) \quad F = \left[M_0 X^l, M_1 X^l, \dots, M_{m-1} X^l \right] \in \mathbb{R}^{n \times c_l m}.$$

The 1D convolution step is accomplished by subsequent multiplication by a learnable weight matrix:

$$(2.4) \quad X^{(l+1)} = \epsilon(FW)$$

with the generalized mixing step $W \in \mathbb{R}^{c_l m \times c_{l+1}}$. The standard GCN using the graph Laplacian can then be viewed as a special case, where $m = 1$ and $M_0 = L$. It is desirable to minimize the number of mixing operators m for a given problem because the number of learnable parameters for a given layer is $c_l \times m \times c_{l+1}$. However, too few mixing operators will be shown to result in reduced accuracy. For this reason, we propose several different predefined sets of mixing operators, such that the network may be tailored to the requirements of the application.

3. Mixing Layers. We propose deriving mixing operators from the spatial gradient operators defined for the underlying spatial discretization. The existence of these gradient operators is a prerequisite to any PDE solution procedure and, thus, should be readily available for any application. Unlike L , these operators should not introduce undesirable dependencies of the learned weights on the local element connectivity. At this time, it is instructive to draw some comparisons to the traditional convolution operator from which we draw inspiration. A 3×3 kernel has 9 parameters, $m = 9$. If we view the image as being defined on a regular rectangular mesh with nodes at the pixel centers, we can compute matrix representations of these operators using a linear finite element basis. For interior nodes, these are equivalent to convolutions with the (unnormalized) kernels shown in [Figure 1](#).

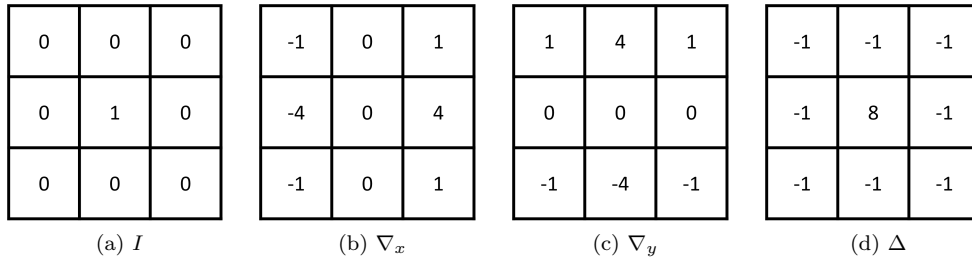


Fig. 1: Differential operators on a regular square mesh are closely related to common filters used for image processing.

There are some differences between how these operators weight contributions at the boundary nodes, compared to the normal approach of zero-padding for traditional CNNs but these differences are not generally significant. Without the inclusion of the identity operator, zero-padding could be viewed as applying a (potentially unphysical) boundary condition to the filtered outputs. With the identity operator, accurate boundary information is able to easily propagate deeper into the network.

Looking at the differential operators in [Figure 1](#), it quickly becomes apparent that a given set of mixing operators defines a linear subspace of the 9-dimensional space spanned by the normal 3×3 convolution kernel. It has been previously observed that learned filters may be represented using a lower dimensional basis as a form of network compression [52]. Visualizing these operators by looking at their stencils is useful for gaining intuition regarding how expressive the resulting network is likely to be. Note, for instance, that the Laplacian $\Delta = \nabla^2$ is a common edge-detection kernel

while ∇_x and ∇_y are closely related to Sobel filters. The L operator from 2.1 is a box blur and may be recovered as a linear combination of the differential operators $L = 9I - \Delta$.

Parameterized differential operators have been previously proposed for various learning tasks including shape classification of meshed surfaces [4, 16] and image classification and segmentation on the unit sphere [28]. While these previous investigations were focused on more restricted application spaces, the operators suggested therein may be more generally applicable. In anisotropic CNNs [4], a patch operator is constructed using anisotropic heat kernels. In our framework, that roughly corresponds to mixing operators of the form

$$(3.1) \quad \nabla \cdot \left(\begin{bmatrix} \delta_{0i} & 0 & 0 \\ 0 & \delta_{1i} & 0 \\ 0 & 0 & \delta_{2i} \end{bmatrix} \nabla \right) i \in \{0, 1, 2\},$$

where δ_{ij} is the Kronecker delta. Parameterized differential operators have also been previously proposed for image classification and segmentation tasks on a unit sphere [28]. In that work, the set of mixing layers was chosen to be $\{I, \nabla_\theta, \nabla_\phi, \nabla^2 = \Delta\}$. The derivative components were chosen to align with the global spherical coordinate system. We will present our proposed mixing operators using cartesian coordinates but application to other coordinate systems is trivial. For our test problems, we have observed that using the derivative operators directly is inadvisable, due to potentially large scale differences between a function and its derivatives. We propose normalizing the derivative operators, such that their absolute value row sums are unity:

$$(3.2) \quad \begin{aligned} \widetilde{\nabla}_x &= D_x^{-1} \nabla_x & (D_x)_{ii} &= \sum_j |(\nabla_x)_{ij}| \\ \widetilde{\nabla}_y &= D_y^{-1} \nabla_y & (D_y)_{ii} &= \sum_j |(\nabla_y)_{ij}| \\ \widetilde{\nabla}_z &= D_z^{-1} \nabla_z & (D_z)_{ii} &= \sum_j |(\nabla_z)_{ij}| \\ \widetilde{\Delta} &= D_\Delta^{-1} \Delta & (D_\Delta)_{ii} &= \sum_j |\Delta_{ij}|. \end{aligned}$$

This type of normalization is common for GCNs. We have also observed performance benefits by further enriching the basis. Specifically, we separate the positive and negative contributions of the gradient operators into separate operators (which is

analogous to adding a learned upwinding parameter), e.g.

$$\begin{aligned}
 (\nabla_x^+)_{ij} &= \begin{cases} 2(D_x^{-1}\nabla_x)_{ij}, & \text{for } (\nabla_x)_{ij} > 0 \\ 0, & \text{otherwise} \end{cases} \\
 (\nabla_x^-)_{ij} &= \begin{cases} -2(D_x^{-1}\nabla_x)_{ij}, & \text{for } (\nabla_x)_{ij} < 0 \\ 0, & \text{otherwise} \end{cases} \\
 (\nabla_y^+)_{ij} &= \begin{cases} 2(D_y^{-1}\nabla_y)_{ij}, & \text{for } (\nabla_y)_{ij} > 0 \\ 0, & \text{otherwise} \end{cases} \\
 (\nabla_y^-)_{ij} &= \begin{cases} -2(D_y^{-1}\nabla_y)_{ij}, & \text{for } (\nabla_y)_{ij} < 0 \\ 0, & \text{otherwise} \end{cases} \\
 (\nabla_z^+)_{ij} &= \begin{cases} 2(D_z^{-1}\nabla_z)_{ij}, & \text{for } (\nabla_z)_{ij} > 0 \\ 0, & \text{otherwise} \end{cases} \\
 (\nabla_z^-)_{ij} &= \begin{cases} -2(D_z^{-1}\nabla_z)_{ij}, & \text{for } (\nabla_z)_{ij} < 0 \\ 0, & \text{otherwise} \end{cases}
 \end{aligned} \tag{3.3}$$

has proven to be valuable in some circumstances.

We therefore have a large set of proposed mixing operators, a subset of which may be used for any given mixing layer. In the examples to follow, we will refer to the following master list (3.4) when specifying the set of mixing operators used in a given layer. For compactness of notation, we omit the explicit scaling of the derivative operators and state that all mixing operators are normalized, such that their row sums are unity. The combinations of mixing operators examined in the experiments to follow will be:

$$\begin{aligned}
 \mathcal{M}_a &= \{I, \Delta_x, \Delta_y\} \\
 \mathcal{M}_b &= \{I, \nabla_x, \nabla_y, \Delta\} \\
 \mathcal{M}_c &= \{I, \nabla_x, \nabla_y, \Delta_x, \Delta_y\} \\
 \mathcal{M}_d &= \{I, \nabla_x^+, \nabla_x^-, \nabla_y^+, \nabla_y^-, \Delta\} \\
 \mathcal{M}_e &= \{I, \nabla_x^+, \nabla_x^-, \nabla_y^+, \nabla_y^-, \Delta_x, \Delta_y\} \\
 \mathcal{M}_f &= \{I\} \\
 \mathcal{M}_g &= \{L\} \\
 \mathcal{M}_h &= \{\Delta\} \\
 \mathcal{M}_i &= \{I, \Delta\}.
 \end{aligned} \tag{3.4}$$

Note that not all possible combinations of these operators are linearly independent (ie. $\nabla_x^+ + \nabla_x^- \propto \nabla_x$), so some care should be taken when selecting operators for a mixing layer to avoid duplication.

4. Network Architectures. Very similar architectures are used for all 3 exemplar problems. The only difference was the depth of the network. For each example, we precompute a sequence of coarsened meshes along with corresponding differential operators and interpolation operators. The network components are then applied at the different mesh resolutions, using the corresponding differential operators and interpolation operators. The fundamental components of the autoencoder networks

are shown in Figure 2. A diagram of the full autoencoder architecture is included in Appendix B. We have observed that the encoder task is significantly less complex than the decoder task for our example applications, which is intuitive, as the decoder task is analogous to solving the system of PDEs whereas the encoder task is analogous to performing a regression to find an unknown parameter from data. As such, we have chosen an asymmetric architecture that devotes a larger number of learned parameters to the decoder task.



Fig. 2: The convolutional autoencoder networks are comprised of 3 fundamental components: the (a) encoder convolutional module, (b) decoder convolutional module, and (c) decoder output module.

The input is fed into the network as a 3D tensor of size $[B, C, N_0]$, where B is the batch size, C is the number of input channels (number of nodal fields), and N_0 is the number of nodes in the input mesh. For each network, a sequence of d progressively

coarser meshes is precomputed with N_0, N_1, \dots, N_d nodes. The encoder network consists of one encoder convolutional module (Figure 2a) for each mesh resolution, a fully connected layer to reduce the size to 64, a nonlinear activation, and another fully connected layer to reduce to the desired latent space dimension d_{latent} , which is treated as a hyper parameter. All nonlinear activation layers use the ELU activation function

$$(4.1) \quad \epsilon(x) = \max(0, x) + \min(0, \alpha(\exp(x) - 1)),$$

with $\alpha = 1$, consistent with previously published results [38]. During experimentation, the choice of nonlinear activation function was not observed to significantly impact the quality of results. For the down-sampling operation, we use the renormalized transpose of the interpolation operator that maps from the coarse mesh to the fine mesh. We will use this same interpolation operator for the upsampling layers in the decoder.

The decoder network begins with 4 fully connected layers. The number of neurons in each layer is 64, $4N_d$, $16N_d$, and $64N_d$, where N_d is the number of nodes in the coarsest mesh. Each fully connected layer is followed by an ELU nonlinear activation layer. These are followed by one decoder convolutional module (Figure 2b) at each mesh resolution save the final (finest) mesh. An output layer (Figure 2c) is used rather than a convolutional layer for the finest mesh. Since no nonlinear activation functions are used in the output layer, the features may be optionally extracted at this point and treated as a nonlinear mode decomposition [46], which is useful for visualization and interpretability. While, in theory, each mixing layer could be comprised of a unique set of mixing operators; in practice, this is cumbersome to manage; so, for each experiment, a common set of mixing operators will be used for all mixing layers.

5. Numerical Experiments. We will be considering three different datasets from a range of computational physics applications. We will be constructing autoencoders and assessing performance in terms of the degree to which the solution lies within the generated manifold. Specifically, we will use the mean-squared error (MSE) between the solution and its reconstruction as our metric. For the experiments to follow, we will vary the sets of mixing operators \mathcal{M} used within the network as well as d_{latent} . The three datasets are:

- Transient advection-diffusion,
- Unsteady laminar fluid flow past a cylinder, and
- Inviscid supersonic flow over a wedge.

The MSE loss function is used for both training and evaluation. This loss function weights the error at each node equally. For regular meshes, this will correspond closely with the L^2 error in the reconstruction. For highly irregular meshes, it may be advisable to use the L^2 or L^1 error directly to avoid over-emphasizing densely meshed regions. In practice, densely meshed regions often correspond to regions of particular interest; therefore, weighting those regions more heavily in the loss calculation may be appropriate in some cases. In addition, the computation of the L^2 or L^1 error is significantly more costly than the MSE. In the following subsections, we will summarize the results of each experiment. Detailed results are tabulated in Appendix A.

5.1. Transient Advection-Diffusion. For our first example, consider the transient, 2D advection-diffusion equation:

$$\begin{aligned}
 \frac{\partial \alpha}{\partial t}(\vec{r}, t) &= \nabla \cdot (D \nabla \alpha(\vec{r}, t)) - \vec{u} \cdot \nabla \alpha(\vec{r}, t) \\
 \vec{r} &\in \Omega \subset \mathbb{R}^2, t \in [0, 1] \\
 \alpha(\vec{r}, 0) &= 0 \\
 \alpha(\vec{r}, t) &= 1 \text{ for } \vec{r} \in \partial\Omega.
 \end{aligned}
 \tag{5.1}$$

The diffusivity D is chosen to be 0.1 and the advection velocity is chosen to be a unit vector, $\|\vec{u}\| = 1$. The equation is solved on the unit square $\Omega = [0, 1] \times [0, 1]$. The direction θ of the advection velocity is varied so $\vec{u} = (\cos(\theta), \sin(\theta))$. Training data is generated every 30° beginning with the positive x -axis ($\theta = 0$). Separate test data is generated for angles of $\theta \in \{45^\circ, 135^\circ, 225^\circ, 315^\circ\}$. The 5 meshes used are regular square meshes of 160×160 , 80×80 , 40×40 , 20×20 , and 10×10 elements apiece.

Referring back to the master list of proposed mixing operators (3.4), we will use all of the proposed mixing operator sets for this experiment. The full results for all combinations of mixing operators, $\mathcal{M} \in \{\mathcal{M}_a, \mathcal{M}_b, \dots, \mathcal{M}_h, \mathcal{M}_i\}$ with $d_{latent} \in \{4, 16, 64\}$ are included in Table 1 in Appendix A. There are also selected results for $d_{latent} = 2$. The results of varying d_{latent} are uneven. In general, increasing d_{latent} should result in a more accurate model. However, since the actual solution manifold for this case is fully contained in \mathbb{R}^2 , it is perhaps expected that increasing d_{latent} beyond 4 fails to continue improving the solution quality. While it is possible to obtain accurate results for $d_{latent} = 2$ for some test problems, the networks suffer in terms of generalizability; a low training loss does not imply low test loss across the board. For POD, the solution continues to improve as expected as d_{latent} is increased. POD accuracy is comparable to the autoencoder results at $d_{latent} = 16$ and nearing machine precision for $d_{latent} = 64$. For ROMs, the online cost is closely related to the cost of solving a least-squares problem (projecting the dynamics onto the solution manifold). The solution is usually generated via an iterative procedure, the cost of which will be problem dependent. If the quadratic Newton-Raphson method is used, the cost of each iteration will scale as $\mathcal{O}(d_{latent}^2)$ [14].

Because the mesh used for this example is a regular grid, a traditional CNN is also used. The architecture is as similar as possible to the autoencoder architecture described in section 4. The same number of convolutional layers with the same number of filters are used and the fully connected layers are identical. The accuracy for both the traditional CNN and proposed extension are comparable indicating that our proposed technique effectively replicates the accuracy of the traditional CNN without relying on any underlying structure in the mesh. Notably, the traditional CNN reconstruction suffers from some high frequency artifacts arising from the upsampling procedure, as shown in Figure 3. While these artifacts have little impact on the integrated accuracy and would likely be smoothed out by LSPG projection of the governing equations in a ROM setting, they are nonetheless worrisome.

The results are more consistently impacted by the choice of mixing operators. For some sets of mixing operators (notably those with lower values of m), the accuracy of the resulting model appears to be highly dependent on the random initialization of the network. Mixing operator set \mathcal{M}_e with $m = 7$ is a consistently well-performing option. Mixing operator sets with $m < 3$ consistently perform worse than those with $m \geq 3$. For this reason, only the 5 sets with $m \geq 3$ will be considered for the other 2

experiments. Operator sets \mathcal{M}_c and \mathcal{M}_e are consistently the top performers, which indicates that value is added by including the anisotropic laplace operators in the mixing operator set for this problem.

Figure 3 compares the reconstructions achieved via convolutional autoencoder (with mixing operator set \mathcal{M}_e), a linear subspace model (POD), and a traditional CNN with a similar autoencoder architecture. The autoencoder-based approaches consistently outperform POD.

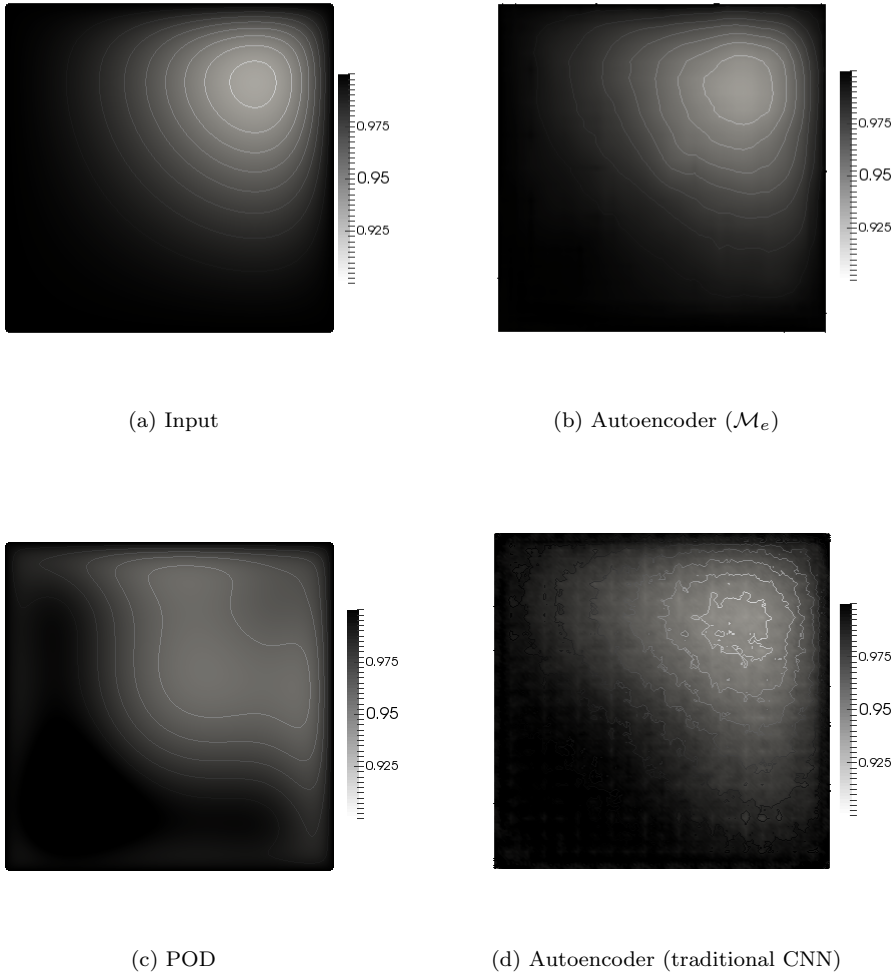


Fig. 3: Distributions of α at the final simulated time ($t = 1$) along with various reconstructions for $\theta = 45$ deg. All reconstructions are performed with $d_{latent} = 4$.

5.2. Unsteady Laminar Fluid Flow Past a Cylinder. The second example involves unsteady laminar flow past a cylinder that generates the familiar vortex shedding pattern known as a von Kármán vortex street. The governing equations for

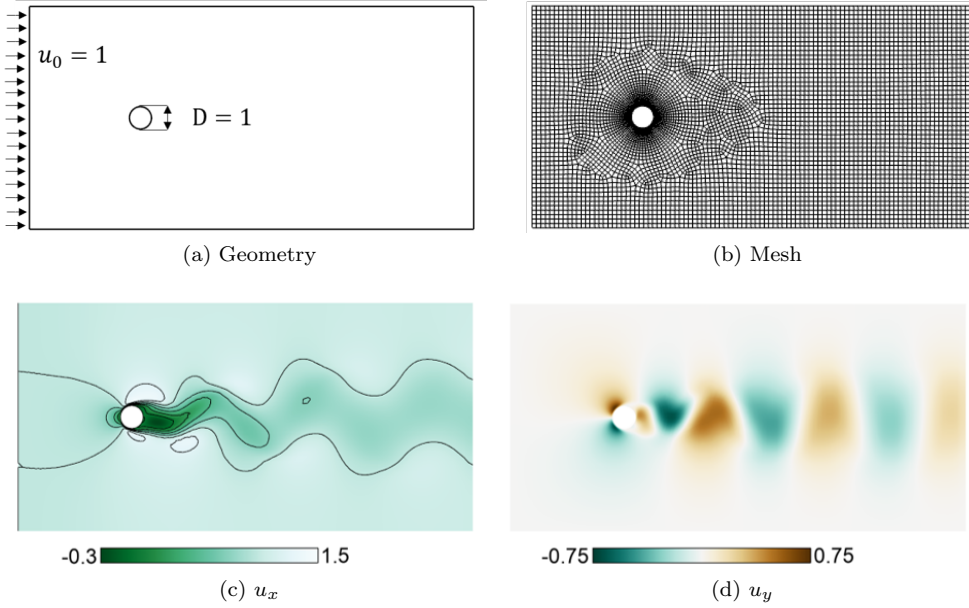


Fig. 4: Unsteady laminar flow past a cylinder (a) has solutions computed on an unstructured mesh (b) which exhibit the familiar vortex shedding patterns visible in the (c) horizontal and (d) vertical velocities.

this system are the incompressible Navier-Stokes equations:

$$(5.2) \quad \begin{aligned} \frac{\partial \vec{u}}{\partial t} + (\vec{u} \cdot \nabla) \vec{u} - \nu \nabla^2 \vec{u} &= 0 \\ \nabla \cdot \vec{u} &= 0. \end{aligned}$$

The geometry is that of a cylinder in cross-flow, as shown in Figure 4. The cylinder has a diameter of 1 and the free stream velocity is 1. The kinematic viscosity ν is varied such that the Reynolds number is between 100 and 400. Symmetry boundary conditions are applied at the top and bottom edges of the domain and an open pressure boundary condition is applied at the outlet. Solutions are generated on an unstructured mesh of 6384 quad elements. Simulations are run with adaptive time stepping with a termination time of 120 resulting in $\mathcal{O}(10^3)$ solution snapshots generated per Reynolds number value. Training data is generated for Reynolds numbers of 100, 200, 300, and 400. Separate test data is generated at a Reynolds numbers of 150, 250, and 350.

Since this example, like the first, is 2D, we will use some of the same sets of mixing operators as before. However, we will limit ourselves to the mixing operators sets that performed best on the advection-diffusion example (those with $m \geq 3$), such that $\mathcal{M} \in \{\mathcal{M}_a, \mathcal{M}_b, \mathcal{M}_c, \mathcal{M}_d, \mathcal{M}_e\}$ and $d_{latent} \in \{2, 4, 16, 64\}$.

The full results for this example are tabulated in Table 2 in Appendix A. The accuracy of the trained autoencoders was insensitive to both of the hyperparameters we varied (within the restricted set of mixing operators considered). There was not a clear winner amongst the mixing operator sets. The ranking varied with both the test dataset considered and the latent space dimension. Additionally, the loss values are

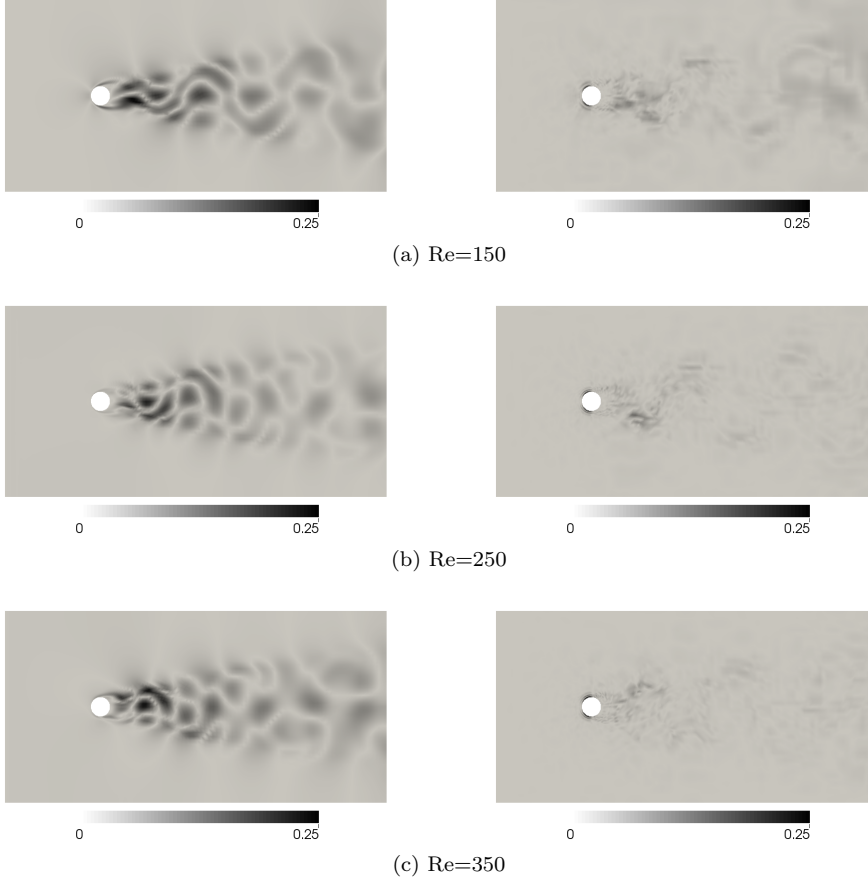


Fig. 5: Absolute error in the horizontal velocity reconstruction at the final timestep for the 3 test datasets using POD (left) and our autoencoder (right) with $d_{latent} = 4$.

all so close together that slightly different training procedures may lead to different relative rankings, indicating that any of the combinations of mixing operators chosen is suitable for this transient laminar flow application. However, operator sets \mathcal{M}_b and \mathcal{M}_d are consistently among the top performers, which indicates that splitting the Laplace operator $\Delta = \Delta_x + \Delta_y$ is likely not worthwhile for this application, possibly due to the invariance of the inlet flow direction across the dataset. Once again, POD achieves comparable accuracy to the autoencoder with $d_{latent} = 16$ and superior accuracy with $d_{latent} = 64$. Figure 5 shows a comparison between the autoencoder and POD for $d_{latent} = 4$. For small values of d_{latent} , our autoencoder is more than an order of magnitude more accurate than POD.

The fact that increasing d_{latent} did not result in increased accuracy indicates that the system's dynamic response is adequately captured by the lower dimensional space, which is not surprising, given that the state evolves on a 2D manifold parameterized by Reynolds number and time. However, as seen in the advection-diffusion example, the existence of a low-dimensional solution manifold is no guarantee that our autoencoder will be able to consistently learn its structure. Minimizing d_{latent} is important in the

context of reduced order modeling as the latent space dimension is one of the primary drivers of online computational cost. For this test problem, our autoencoder is able to consistently learn a minimal representation of the solution manifold.

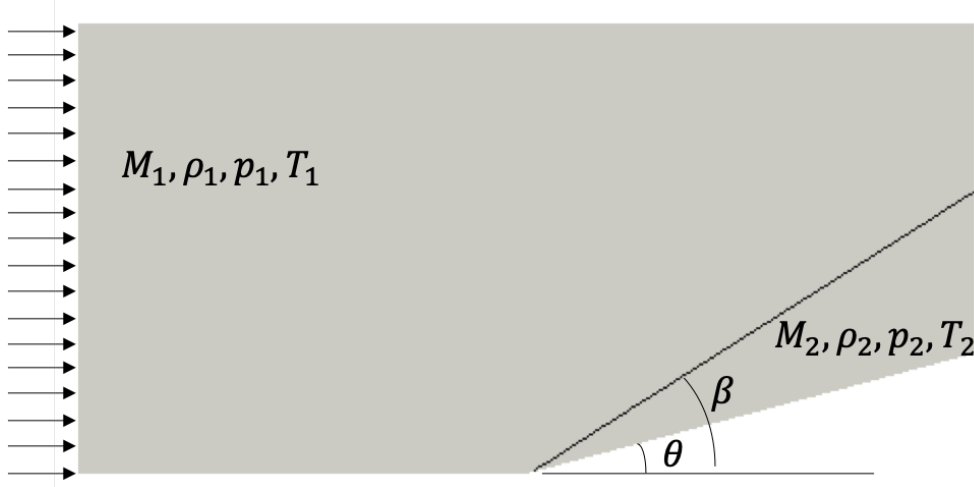


Fig. 6: Steady inviscid supersonic flow over a wedge results in an oblique shock originating at the corner. The flow state is piecewise constant with the inlet and outlet conditions shown.

5.3. Inviscid Supersonic Flow Over a Wedge. The third and final experiment involves steady, 2D supersonic inviscid flow. The geometry includes a surface with a sharp corner turning into the flow to induce an oblique shock, as shown in Figure 6. The angle of the wall is $\theta = \text{deg } 15$. The governing equations

$$\begin{aligned}
 (5.3) \quad & \frac{\partial \rho}{\partial t} + \nabla \cdot (\rho \vec{u}) = 0, \\
 & \frac{\partial (\rho \vec{u})}{\partial t} + \nabla \cdot (\rho \vec{u} \vec{u}^T) + \nabla P = 0, \text{ and} \\
 & \frac{\partial (\rho E)}{\partial t} + \nabla \cdot (\rho H \vec{u}) = 0
 \end{aligned}$$

are the inviscid Euler equations (enforcing conservation of mass, momentum, and energy), with H as the total enthalpy and E as the total internal energy. The equations are closed using the ideal gas law $P = \rho RT/M$.

The inflow boundary conditions are fixed as constant values. A symmetry boundary condition is prescribed along the bottom surface and open flow boundary conditions are prescribed along the top and right (outflow) surfaces. The problem is initialized with the inflow conditions and pseudo-timestepping is used to achieve steady-state. The inflow pressure and temperature are chosen to be $p_1 = 101352.93$ and $T_1 = 288.89$, respectively. The free stream Mach number M_1 is varied across training and testing scenarios. A shock forms at angle β to the flow where the wall turns sharply into the flow at the corner. θ and β are related to M_1 by the $\theta - \beta - M$

equation:

$$(5.4) \quad \tan \theta = 2 \cot \beta \frac{M_1^2 \sin^2 \beta - 1}{M_1^2 (\gamma + \cos 2\beta) + 2}.$$

Once β is computed from (5.4), the downstream conditions can be computed from the following equations:

$$(5.5) \quad \begin{aligned} \frac{p_2}{p_1} &= 1 + \frac{2\gamma}{\gamma+1} (M_1^2 \sin^2 \beta - 1), \\ \frac{\rho_2}{\rho_1} &= \frac{(\gamma+1)M_1^2 \sin^2 \beta}{(\gamma-1)M_1^2 \sin^2 \beta + 2}, \\ \frac{T_2}{T_1} &= \frac{p_2}{p_1} \frac{\rho_1}{\rho_2}, \text{ and} \\ M_2 &= \frac{1}{\sin(\beta - \theta)} \left(\frac{1 + \frac{\gamma-1}{2} M_1^2 \sin^2 \beta}{\gamma M_1^2 \sin^2 \beta - \frac{\gamma-1}{2}} \right)^{1/2}. \end{aligned}$$

The conditions ahead of and behind the shock are then given by $\{M_1, \rho_1, p_1, T_1\}$ and $\{M_2, \rho_2, p_2, T_2\}$ respectively. The local sound speed is given by $c = \sqrt{\gamma p / \rho}$. From the sound speed, the air speed $V = Mc = M\sqrt{\gamma p / \rho}$ can be computed. Therefore, the velocity field is $\mathbf{v} = (u_1, 0)$ ahead of the shock and $\mathbf{v} = (u_2 \cos(\theta), u_2 \sin(\theta))$ behind the shock, where $u_i = M_i \sqrt{\gamma p_i / \rho_i}$ and $i = 1, 2$.

The domain is discretized using 12800 quad elements and training data is generated for $M_1 \in \{2, 2.1, 2.2, \dots, 5.9, 6.0\}$. Separate test data is generated for $M_1 \in \{2.25, 3.25, 4.25, 5.25\}$.

We will use the same mixing operator sets as in the laminar flow experiment $\mathcal{M} \in \{\mathcal{M}_a, \mathcal{M}_b, \mathcal{M}_c, \mathcal{M}_d, \mathcal{M}_e\}$. Full results are tabulated in Table 3 in Appendix A. The 41 datapoints used for training in this case are considerably fewer than those used for the other experiments, owing to the fact that significantly less information is harvested from a steady-state solution than from a transient solution. The data could theoretically be augmented by inclusion of pseudo-timestepping data generated during the solution process, but doing so proved unnecessary in this case. However, only having 41 training points restricts the maximum latent dimension of the POD reconstruction to no more than 41.

All 5 mixing operator sets performed comparably for this experiment, and the autoencoder outperformed the POD reconstruction over the full range of Mach numbers considered for $d_{latent} \leq 8$. This problem is especially challenging for linear subspace methods such as POD, owing to the exceptionally slow decay of the Kolmogorov n -width. The POD reconstruction includes large oscillations that pollute the solution both upwind and downwind of the shock. These oscillations persist (especially for lower Mach numbers) until a relatively large number of modes are retained ($d_{latent} > 16$). In contrast, the autoencoder reconstruction error is localized around the shock front. For the density reconstruction pictured in Figure 7, the amplitude of these errors increases with increasing M_1 , but only at a rate commensurate with the increase of ρ_2 . The autoencoder is able to reconstruct the field data with a very small latent space. Little performance degradation is seen, even for $d_{latent} = 1$, in which case the autoencoder has precisely learned the solution manifold for this problem.

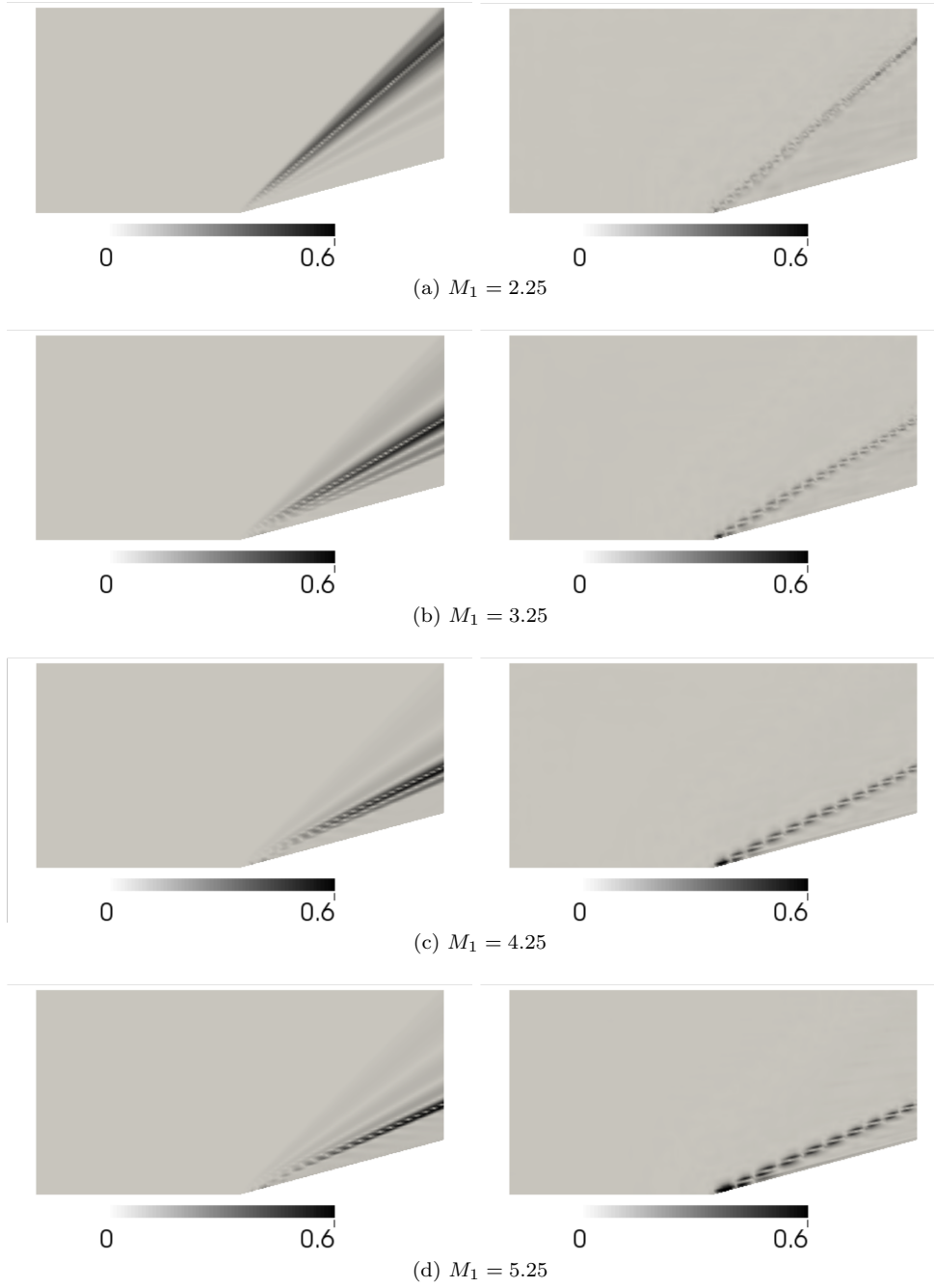


Fig. 7: Absolute error in the density reconstruction for the 4 test points using POD (left) and our autoencoder (right) with equivalent latent space dimension ($d_{latent} = 4$).

6. Conclusions. We combined the traditional CNNs ability to learn physically relevant filters with the GCNs applicability to unstructured meshes, allowing us to accurately reconstruct the nonlinear solution manifolds of PDEs, which had previously proven challenging for projection-based ROMs. Our approach achieves an order of magnitude improvement in accuracy relative to linear subspace methods for the 3 selected exemplar problems. The accuracy is comparable to that achieved by a traditional CNN autoencoder for the transient advection-diffusion problem for which both are applicable. For the other 2 example problems, the traditional CNN is unable to deal with the lack of structure in the spatial discretization, but our proposed approach continues to achieve similar gains in accuracy relative to POD enabling low-cost ROMs of systems that previously required a much higher latent space dimension.

The proposed networks represent an extension of CNNs to the processing of data represented using unstructured spatial discretizations. Doing so significantly increases the applicability of CNNs, due to the resulting support for arbitrarily complex geometries. The only prerequisite is the ability to compute the required differential and interpolation operators, which should be readily available for any discretization used for the solution of PDEs (including meshless methods). In our implementation, these operators are precomputed, but they could also be computed at run time, which would be useful if training/test data include a variety of spatial discretizations, but would come with additional computational overhead. The extension of the powerful CNN technique to these types of data is important, not only in that it enables nonlinear projection-based ROMs on arbitrarily complex geometries, but also that it enables other tasks requiring low-dimensional embeddings of computational data (e.g. synthesizing computational and experimental data, data compression, or surrogate modeling) for complex systems.

The choice of mixing operators is shown to have limited impact on the ultimate accuracy of the method, although highly restrictive sets ($m < 3$) exhibited markedly worse accuracy. For the 3 different experiments, different mixing operator sets were shown to be advantageous. For the advection-diffusion experiment, operator set \mathcal{M}_e was generally best; for the laminar flow experiment, operator set \mathcal{M}_d was generally best; and for the inviscid Euler experiment, operator set \mathcal{M}_b was generally best. This difference indicates a problem-dependent nature to the optimal choice of mixing operators. Additionally, more expressive operator sets are observed to usually (although not always) result in easier training. For the examples considered, the solutions evolve along low-dimensional manifolds, which are able to be successfully represented with $d_{latent} \leq 4$. Further increasing the latent space dimension did not generally result in increased accuracy. Larger latent spaces may be required for different datasets, but it is expected that d_{latent} should not be required to exceed the dimensionality of the underlying solution manifold by much, if at all, which is consistent with prior findings on the use of deep autoencoders to construct nonlinear trial subspaces for projection-based ROMs [38, 39]. A similar network architecture was used for all 3 experiments and minimal effort was made to optimize it. It is expected that further accuracy improvements are possible if the architecture is tailored to a particular dataset.

All of the datasets examined here were 2D. However, as noted in [section 3](#), the extension to 3D is trivial. Additionally, the transition from 2D to 3D when using our proposed mixing operator sets is significantly less costly than for traditional CNNs, corresponding to an increase in the number of learnable parameters per convolutional layer of between 25% and 43% depending on the mixing operator set relative to the

200% required for traditional CNNs.

Appendix A. Tables of Loss Values. Here, we include detailed summaries of the accuracy achieved in all three experiments, for every value of each hyperparameter considered. In each case, the 'loss' refers to the MSE loss of the solution which is closely related to the L^2 error in the reconstruction. However, the precise relationship between the loss and the L^2 error is mesh- and dataset-dependent, and the loss values reported here are unnormalized. Consequently, while the loss is valuable for comparing the results across hyperparameter space for a single experiment, direct comparisons between experiments are not valid. Therefore, the fact that the loss values in [Table 1](#) are generally lower than those in [Table 2](#) does not imply that the reconstructions are more accurate for the advection diffusion experiment than for the laminar flow experiment. For convenience, the most accurate set of mixing operators for each test and for each value of d_{latent} is highlighted. In those cases where POD was more accurate than the autoencoder, those results are also highlighted.

Table 1: Loss performance for transient advection-diffusion experiment.

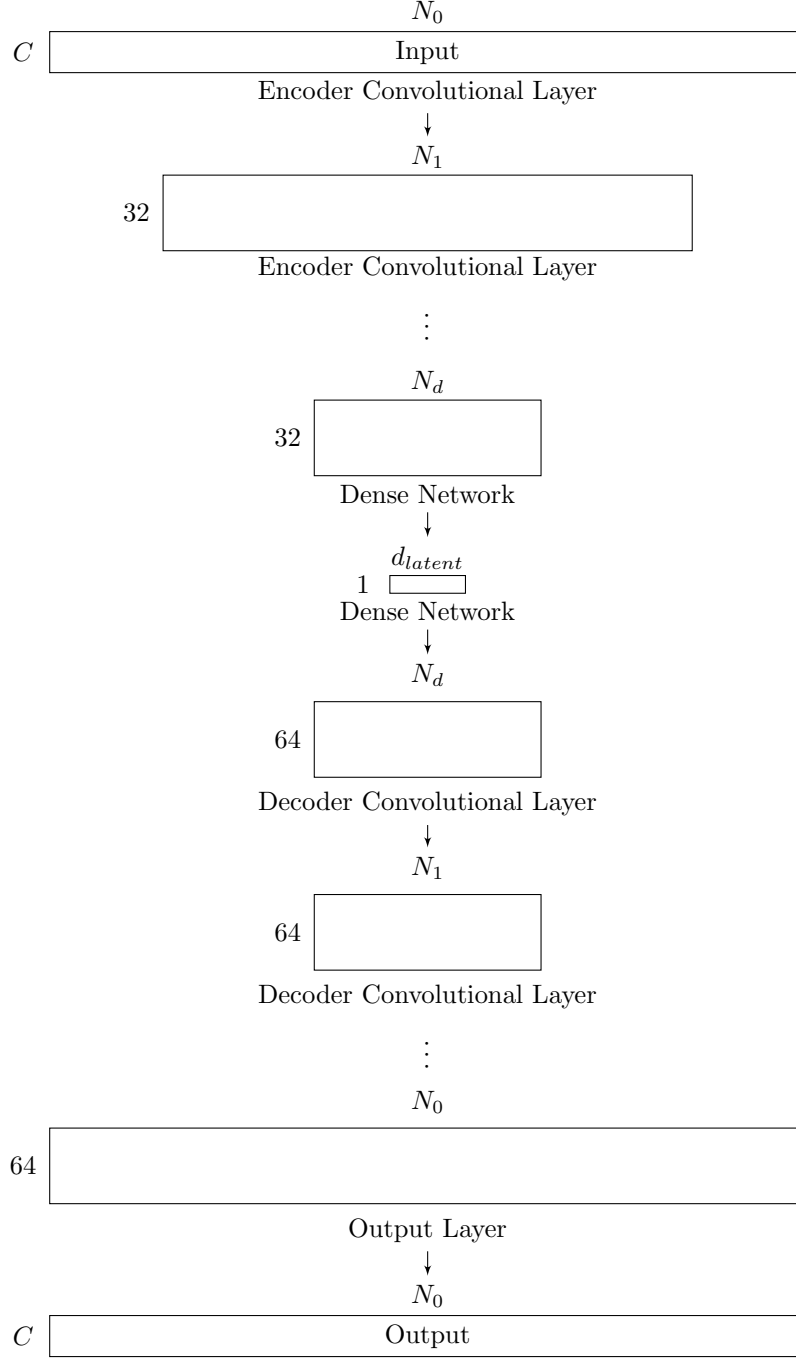
	Mixing Set	Training Loss	Test Loss			
			$\theta = 45^\circ$	$\theta = 135^\circ$	$\theta = 225^\circ$	$\theta = 315^\circ$
$d_{latent} = 2$	(a)	1.246e-5	7.828e-6	3.759e-6	1.868e-5	1.036e-3
	(b)	9.524e-5	4.199e-2	1.208e-2	1.765e-4	1.711e-2
	(c)	1.596e-5	5.159e-6	1.056e-2	6.170e-4	2.219e-5
	(d)	1.261e-5	3.217e-2	8.677e-6	4.880e-6	1.623e-4
	(e)	1.335e-5	7.714e-6	8.158e-6	2.840e-3	1.048e-2
$d_{latent} = 4$	(a)	4.116e-5	7.339e-6	8.486e-6	1.102e-5	7.708e-6
	(b)	5.994e-5	1.286e-5	1.027e-5	9.766e-6	1.067e-5
	(c)	7.141e-5	1.906e-5	2.149e-5	1.269e-5	1.577e-5
	(d)	4.083e-5	1.425e-5	1.046e-5	7.233e-6	2.288e-5
	(e)	2.273e-5	7.048e-6	5.419e-6	4.553e-6	4.967e-6
	(f)	2.221e-4	3.289e-5	3.338e-5	3.274e-5	3.458e-5
	(g)	4.592e-4	6.978e-5	6.587e-5	6.787e-5	6.627e-5
	(h)	9.388e-1	1.345e-1	1.345e-1	1.345e-1	1.345e-1
	(i)	1.645e-3	2.442e-4	2.352e-4	3.084e-4	2.285e-4
	POD	1.198e-2	1.456e-3	1.456e-3	1.456e-3	1.456e-3
	CNN	2.770e-5	3.523e-5	3.456e-5	3.599e-5	3.608e-5
$d_{latent} = 16$	(a)	2.305e-4	3.982e-5	4.294e-5	3.205e-5	4.031e-5
	(b)	7.178e-5	1.164e-5	1.169e-5	1.144e-5	1.181e-5
	(c)	9.102e-6	2.828e-6	9.565e-6	4.527e-6	3.649e-6
	(d)	4.203e-5	1.194e-5	1.057e-5	1.095e-5	1.050e-5
	(e)	9.437e-6	1.005e-5	7.028e-6	5.801e-6	9.888e-6
	(f)	9.388e-1	1.345e-1	1.345e-1	1.345e-1	1.345e-1
	(g)	5.791e-1	8.338e-2	8.239e-2	8.353e-2	8.181e-2
	(h)	9.388e-1	1.345e-1	1.345e-1	1.345e-1	1.345e-1
	(i)	8.142e-5	1.378e-5	1.781e-5	2.017e-5	1.397e-5
	POD	7.096e-5	6.973e-6	6.973e-6	6.973e-6	6.973e-6
	CNN	3.817e-5	4.797e-5	4.589e-5	5.064e-5	4.728e-5
$d_{latent} = 64$	(a)	1.203e-5	4.078e-6	7.811e-6	5.454e-6	6.364e-6
	(b)	7.620e-5	1.188e-5	1.505e-5	1.392e-5	1.410e-5
	(c)	2.376e-5	3.756e-6	1.024e-5	9.465e-6	3.630e-5
	(d)	2.064e-4	3.063e-5	3.011e-5	3.036e-5	3.010e-5
	(e)	1.995e-5	3.676e-6	4.691e-6	4.461e-6	5.268e-6
	(f)	7.820e-2	1.120e-2	1.122e-2	1.120e-2	1.119e-2
	(g)	1.663e-4	2.549e-5	2.357e-5	3.691e-5	2.415e-5
	(h)	9.388e-2	1.344e-1	1.345e-1	1.345e-1	1.345e-1
	(i)	4.366e-2	1.824e-3	1.003e-2	1.623e-3	1.122e-2
	POD	1.002e-9	1.277e-10	1.274e-10	1.274e-10	1.275e-10
	CNN	2.872e-5	3.978e-5	3.923e-5	3.937e-5	3.843e-5

Table 2: Loss performance for laminar flow experiment.

	Mixing Set	Training Loss	Test Loss		
			$Re = 150$	$Re = 250$	$Re = 350$
$d_{latent} = 2$	(a)	5.382e-3	7.992e-3	4.112e-3	5.629e-3
	(b)	4.892e-3	9.909e-3	3.848e-3	3.024e-3
	(c)	5.126e-3	8.562e-3	4.563e-3	3.243e-3
	(d)	4.968e-3	9.522e-3	3.893e-3	2.859e-3
	(e)	5.009e-3	9.245e-3	5.767e-3	2.986e-3
$d_{latent} = 4$	(a)	4.002e-3	9.01e-4	1.668e-3	1.678e-3
	(b)	3.940e-3	8.56e-4	1.765e-3	1.638e-3
	(c)	4.182e-3	9.62e-4	1.903e-3	1.787e-3
	(d)	3.979e-3	7.21e-4	1.638e-3	1.627e-3
	(e)	4.029e-3	8.07e-4	1.681e-3	1.681e-3
	POD	1.186e-1	2.604e-2	2.465e-2	3.195e-2
$d_{latent} = 16$	(a)	4.034e-3	6.23e-4	1.256e-3	1.643e-3
	(b)	3.970e-3	5.68e-4	1.202e-3	1.608e-3
	(c)	4.168e-3	6.84e-4	1.356e-3	1.675e-3
	(d)	3.904e-3	5.89e-4	1.211e-3	1.592e-3
	(e)	4.079e-3	6.14e-4	1.253e-3	1.653e-3
	POD	1.831e-2	4.062e-3	4.418e-3	5.144e-3
$d_{latent} = 64$	(a)	4.034e-3	7.98e-4	1.454e-3	1.664e-3
	(b)	3.903e-3	5.66e-4	1.194e-3	1.589e-3
	(c)	4.078e-3	6.90e-4	1.348e-3	1.666e-3
	(d)	3.872e-3	5.60e-4	1.165e-3	1.576e-3
	(e)	3.975e-3	6.44e-4	1.273e-3	1.633e-3
	POD	7.534e-4	2.780e-4	4.163e-4	2.665e-4

Table 3: Loss performance for inviscid Euler experiment.

	Mixing Set	Training Loss	Test Loss			
			$M_1 = 2.25$	$M_1 = 3.25$	$M_1 = 4.25$	$M_1 = 5.25$
$d_{latent} = 1$	(a)	1.276e-3	2.245e-4	4.518e-4	1.089e-3	2.384e-3
	(b)	1.267e-3	1.816e-4	4.354e-4	1.081e-3	2.380e-3
	(c)	1.387e-3	4.687e-4	5.062e-4	1.143e-3	2.460e-3
	(d)	1.338e-3	2.020e-4	4.660e-4	1.143e-3	2.483e-3
	(e)	1.330e-3	3.502e-4	4.951e-4	1.124e-3	2.426e-3
	POD	1.545e-2	2.408e-2	1.647e-2	1.551e-2	5.330e-3
$d_{latent} = 2$	(a)	1.275e-3	2.578e-4	4.445e-4	1.085e-3	2.383e-3
	(b)	1.257e-3	2.004e-4	4.302e-4	1.074e-3	2.375e-3
	(c)	1.286e-3	2.410e-4	4.564e-4	1.100e-3	2.405e-3
	(d)	1.308e-3	2.454e-4	4.659e-4	1.111e-3	2.413e-3
	(e)	1.333e-3	2.472e-4	4.712e-4	1.123e-3	2.446e-3
	POD	8.293e-3	9.475e-3	1.000e-2	7.595e-3	2.883e-3
$d_{latent} = 3$	(a)	1.262e-3	1.986e-4	4.371e-4	1.079e-3	2.375e-3
	(b)	1.255e-3	1.681e-4	4.280e-4	1.073e-3	2.372e-3
	(c)	1.260e-3	1.959e-4	4.352e-4	1.078e-3	2.375e-3
	(d)	1.299e-3	2.052e-4	4.658e-4	1.109e-3	2.426e-3
	(e)	1.336e-3	3.871e-4	5.028e-4	1.117e-3	2.408e-3
	POD	5.165e-3	6.082e-3	4.760e-3	3.088e-3	2.875e-3
$d_{latent} = 4$	(a)	1.265e-3	2.306e-4	4.368e-4	1.081e-3	2.378e-3
	(b)	1.256e-3	1.741e-4	4.290e-4	1.074e-3	2.373e-3
	(c)	1.263e-3	1.994e-4	4.366e-4	1.080e-3	2.378e-3
	(d)	1.283e-3	2.066e-4	4.472e-4	1.096e-3	2.402e-3
	(e)	1.346e-3	3.836e-4	5.154e-4	1.139e-3	2.453e-3
	POD	3.485e-3	5.833e-3	4.447e-3	3.030e-3	2.549e-3
$d_{latent} = 8$	(a)	1.288e-3	2.529e-4	4.611e-4	1.093e-3	2.392e-3
	(b)	1.261e-3	1.838e-4	4.322e-4	1.077e-3	2.376e-3
	(c)	1.264e-3	2.160e-4	4.402e-4	1.079e-3	2.376e-3
	(d)	1.324e-3	2.287e-4	4.804e-4	1.132e-3	2.425e-3
	(e)	1.381e-3	4.518e-4	5.243e-4	1.167e-3	2.441e-3
	POD	1.041e-3	2.184e-3	1.308e-3	8.682e-4	3.932e-4
$d_{latent} = 16$	(a)	1.265e-3	1.967e-4	4.383e-4	1.078e-3	2.379e-3
	(b)	1.256e-3	1.739e-4	4.289e-4	1.073e-3	2.372e-3
	(c)	1.263e-3	1.986e-4	4.350e-4	1.083e-3	2.381e-3
	(d)	1.350e-3	4.819e-4	4.903e-4	1.127e-3	2.420e-3
	(e)	1.315e-3	3.467e-4	4.716e-4	1.105e-3	2.406e-3
	POD	1.450e-4	7.975e-4	1.855e-4	1.164e-4	1.037e-4
$d_{latent} = 32$	(a)	1.268e-3	2.165e-4	4.402e-4	1.081e-3	2.381e-3
	(b)	1.260e-3	1.812e-4	4.321e-4	1.076e-3	2.375e-3
	(c)	1.260e-3	2.193e-4	4.402e-4	1.079e-3	2.375e-3
	(d)	1.276e-3	2.149e-4	4.471e-4	1.090e-3	2.389e-3
	(e)	1.290e-3	2.503e-4	4.629e-4	1.100e-3	2.395e-3
	POD	4.239e-7	7.300e-4	9.189e-6	1.367e-6	1.203e-6
$d_{latent} = 64$	(a)	1.262e-3	1.934e-4	4.346e-4	1.077e-3	2.376e-3
	(b)	1.262e-3	2.257e-4	4.354e-4	1.078e-3	2.376e-3
	(c)	1.262e-3	1.898e-4	4.361e-4	1.080e-3	2.379e-3
	(d)	1.361e-3	2.995e-4	5.170e-4	1.150e-3	2.481e-3
	(e)	1.265e-3	1.966e-4	4.376e-4	1.080e-3	2.377e-3

Appendix B. Network Architecture.

Acknowledgments. Supported by the Laboratory Directed Research and Development program at Sandia National Laboratories, a multimission laboratory managed and operated by National Technology and Engineering Solutions of Sandia LLC, a wholly owned subsidiary of Honeywell International Inc. for the U.S. Department of Energys National Nuclear Security Administration under contract DE-NA0003525.

REFERENCES

- [1] C. BEATTIE AND S. GUGERCIN, *Model Reduction by Rational Interpolation*, ch. 7, pp. 297–334, <https://doi.org/10.1137/1.9781611974829.ch7>, <https://epubs.siam.org/doi/abs/10.1137/1.9781611974829.ch7>, <https://arxiv.org/abs/https://epubs.siam.org/doi/pdf/10.1137/1.9781611974829.ch7>.
- [2] P. BENNER, S. GUGERCIN, AND K. WILLCOX, *A survey of projection-based model reduction methods for parametric dynamical systems*, 2015.
- [3] P. BENNER, P. KRŠCHNER, AND J. SAAK, *Frequency-limited balanced truncation with low-rank approximations*, SIAM Journal on Scientific Computing, 38 (2016), pp. A471–A499, <https://doi.org/10.1137/15M1030911>, <https://doi.org/10.1137/15M1030911>, <https://arxiv.org/abs/https://doi.org/10.1137/15M1030911>.
- [4] D. BOSCAINI, J. MASCI, E. RODOL, AND M. M. BRONSTEIN, *Learning shape correspondence with anisotropic convolutional neural networks*, 2016, <https://arxiv.org/abs/1605.06437>.
- [5] J. BRUNA, W. ZAREMBA, A. SZLAM, AND Y. LECUN, *Spectral networks and locally connected networks on graphs*, (2013), <https://arxiv.org/abs/1312.6203>.
- [6] K. CARLBERG, C. BOU-MOSLEH, AND C. FARHAT, *Efficient non-linear model reduction via a least-squares petrov-galerkin projection and compressive tensor approximations*, International Journal for Numerical Methods in Engineering, 86, pp. 155–181, <https://doi.org/10.1002/nme.3050>, <https://onlinelibrary.wiley.com/doi/abs/10.1002/nme.3050>, <https://arxiv.org/abs/https://onlinelibrary.wiley.com/doi/pdf/10.1002/nme.3050>.
- [7] K. CARLBERG, C. FARHAT, J. CORTIAL, AND D. AMSALLEM, *The gnat method for nonlinear model reduction: Effective implementation and application to computational fluid dynamics and turbulent flows*, Journal of Computational Physics, 242 (2013), pp. 623 – 647, <https://doi.org/https://doi.org/10.1016/j.jcp.2013.02.028>, <http://www.sciencedirect.com/science/article/pii/S0021999113001472>.
- [8] K. T. CARLBERG, A. JAMESON, M. J. KOCHENDERFER, J. MORTON, L. PENG, AND F. D. WITHERDEN, *Recovering missing cfd data for high-order discretizations using deep neural networks and dynamics learning*, Journal of Computational Physics, 395 (2019), pp. 105 – 124, <https://doi.org/https://doi.org/10.1016/j.jcp.2019.05.041>, <http://www.sciencedirect.com/science/article/pii/S0021999119303857>.
- [9] F. CHINESTA, P. LADEVÈZE, AND E. CUETO, *A short review on model order reduction based on proper generalized decomposition*, Archives of Computational Methods in Engineering, 18 (2011), pp. 395–404.
- [10] V. DAS, A. POLLACK, U. WOLLNER, AND T. MUKERJI, *Convolutional neural network for seismic impedance inversion*, 08 2018, pp. 2071–2075, <https://doi.org/10.1190/segam2018-2994378.1>.
- [11] C. DONG, C. C. LOY, AND X. TANG, *Accelerating the super-resolution convolutional neural network*, in Computer Vision – ECCV 2016, B. Leibe, J. Matas, N. Sebe, and M. Welling, eds., Cham, 2016, Springer International Publishing, pp. 391–407.
- [12] C. DOS SANTOS AND M. GATTI, *Deep convolutional neural networks for sentiment analysis of short texts*, in Proceedings of COLING 2014, the 25th International Conference on Computational Linguistics: Technical Papers, Dublin, Ireland, Aug. 2014, Dublin City University and Association for Computational Linguistics, pp. 69–78, <https://www.aclweb.org/anthology/C14-1008>.
- [13] F. EBERT AND T. STYKEL, *Rational interpolation, minimal realization and model reduction*. 2007.
- [14] M. ERDOGDU, M. BAYATI, AND L. DICKER, *Scaled least squares estimator for glms in large-scale problems*, Advances in Neural Information Processing Systems, (2016), pp. 3332–3340. 30th Annual Conference on Neural Information Processing Systems, NIPS 2016 ; Conference date: 05-12-2016 Through 10-12-2016.
- [15] A. B. FARIMANI, J. GOMES, AND V. S. PANDE, *Deep learning the physics of transport phenomena*, CoRR, abs/1709.02432 (2017), <http://arxiv.org/abs/1709.02432>, <https://arxiv.org/abs/1709.02432>.
- [16] M. FEY, J. E. LENSSEN, F. WEICHERT, AND H. MLLER, *Splinecnn: Fast geometric deep learning with continuous b-spline kernels*, (2017), <https://arxiv.org/abs/1711.08920>.
- [17] S. FRESCA, L. DEDE, AND A. MANZONI, *A comprehensive deep learning-based approach to reduced order modeling of nonlinear time-dependent parametrized pdes*, 2020, <https://arxiv.org/abs/2001.04001>.
- [18] Z. GONG, P. ZHONG, Y. YU, W. HU, AND S. LI, *A cnn with multiscale convolution and diversified metric for hyperspectral image classification*, IEEE Transactions on Geoscience and Remote Sensing, 57 (2019), pp. 3599–3618, <https://doi.org/10.1109/TGRS.2018.2886022>.

- [19] F. J. GONZALEZ AND M. BALAJEWICZ, *Deep convolutional recurrent autoencoders for learning low-dimensional feature dynamics of fluid systems*, 2018, <https://arxiv.org/abs/1808.01346>.
- [20] C. GRLE, M. HINZE, AND S. VOLKWEIN, *Model order reduction by proper orthogonal decomposition*, 2019, <https://arxiv.org/abs/1906.05188>.
- [21] S. GUGERCIN AND A. C. ANTOULAS, *A survey of model reduction by balanced truncation and some new results*, International Journal of Control, 77 (2004), pp. 748–766, <https://doi.org/10.1080/00207170410001713448>, <https://doi.org/10.1080/00207170410001713448>, <https://arxiv.org/abs/https://doi.org/10.1080/00207170410001713448>.
- [22] X. GUO, W. LI, AND F. IORIO, *Convolutional neural networks for steady flow approximation*, in Proceedings of the 22nd ACM SIGKDD International Conference on Knowledge Discovery and Data Mining, KDD 16, New York, NY, USA, 2016, Association for Computing Machinery, p. 481490, <https://doi.org/10.1145/2939672.2939738>, <https://doi.org/10.1145/2939672.2939738>.
- [23] T. HAMAGUCHI, H. OIWA, M. SHIMBO, AND Y. MATSUMOTO, *Knowledge base completion with out-of-knowledge-base entities: A graph neural network approach*, Transactions of the Japanese Society for Artificial Intelligence, 33 (2018), p. 110, <https://doi.org/10.1527/tjsai.f-h72>, <http://dx.doi.org/10.1527/tjsai.F-H72>.
- [24] W. L. HAMILTON, R. YING, AND J. LESKOVEC, *Inductive representation learning on large graphs*, 2017, <https://arxiv.org/abs/1706.02216>.
- [25] M. HEINKENSCHLOSS, T. REIS, AND A. ANTOULAS, *Balanced truncation model reduction for systems with inhomogeneous initial conditions*, Automatica, 47 (2011), pp. 559 – 564, <https://doi.org/https://doi.org/10.1016/j.automatica.2010.12.002>, <http://www.sciencedirect.com/science/article/pii/S0005109810004905>.
- [26] M. HENAFF, J. BRUNA, AND Y. LECUN, *Deep convolutional networks on graph-structured data*, (2015), <https://arxiv.org/abs/1506.05163>.
- [27] B. HU, Z. LU, H. LI, AND Q. CHEN, *Convolutional neural network architectures for matching natural language sentences*, in Advances in Neural Information Processing Systems 27, Z. Ghahramani, M. Welling, C. Cortes, N. D. Lawrence, and K. Q. Weinberger, eds., Curran Associates, Inc., 2014, pp. 2042–2050, <http://papers.nips.cc/paper/5550-convolutional-neural-network-architectures-for-matching-natural-language-sentences.pdf>.
- [28] C. M. JIANG, J. HUANG, K. KASHINATH, PRABHAT, P. MARCUS, AND M. NIESSNER, *Spherical CNNs on unstructured grids*, in International Conference on Learning Representations, 2019, <https://openreview.net/forum?id=Bkl-43C9FQ>.
- [29] N. KALCHBRENNER, E. GREFFENSTETTE, AND P. BLUNSOM, *A convolutional neural network for modelling sentences*, CoRR, abs/1404.2188 (2014), <http://arxiv.org/abs/1404.2188>, <https://arxiv.org/abs/1404.2188>.
- [30] A. KAPPELER, S. YOO, Q. DAI, AND A. K. KATSAGGELOS, *Video super-resolution with convolutional neural networks*, IEEE Transactions on Computational Imaging, 2 (2016), pp. 109–122, <https://doi.org/10.1109/TCI.2016.2532323>.
- [31] G. KERSCHEN, J. CLAUDE GOLINVAL, A. F. VAKAKIS, AND L. A. BERGMAN, *The method of proper orthogonal decomposition for dynamical characterization and order reduction of mechanical systems: an overview*, Nonlinear Dynamics, (2005), pp. 147–169.
- [32] J. KIM, J. KWON LEE, AND K. MU LEE, *Accurate image super-resolution using very deep convolutional networks*, in The IEEE Conference on Computer Vision and Pattern Recognition (CVPR), June 2016.
- [33] T. N. KIPF AND M. WELLING, *Semi-supervised classification with graph convolutional networks*, 2016, <https://arxiv.org/abs/1609.02907>.
- [34] A. KRIZHEVSKY, I. SUTSKEVER, AND G. E. HINTON, *Imagenet classification with deep convolutional neural networks*, in Advances in Neural Information Processing Systems 25, F. Pereira, C. J. C. Burges, L. Bottou, and K. Q. Weinberger, eds., Curran Associates, Inc., 2012, pp. 1097–1105, <http://papers.nips.cc/paper/4824-imagenet-classification-with-deep-convolutional-neural-networks.pdf>.
- [35] A. KRIZHEVSKY, I. SUTSKEVER, AND G. E. HINTON, *Imagenet classification with deep convolutional neural networks*, Commun. ACM, 60 (2017), p. 8490, <https://doi.org/10.1145/3065386>, <https://doi.org/10.1145/3065386>.
- [36] S. LAWRENCE, C. L. GILES, AH CHUNG TSOI, AND A. D. BACK, *Face recognition: a convolutional neural-network approach*, IEEE Transactions on Neural Networks, 8 (1997), pp. 98–113, <https://doi.org/10.1109/72.554195>.
- [37] Y. LECUN AND Y. BENGIO, *Convolutional networks for images, speech, and time-series*, MIT Press, 1995.

- [38] K. LEE AND K. CARLBERG, *Model reduction of dynamical systems on nonlinear manifolds using deep convolutional autoencoders*, 2018, <https://arxiv.org/abs/1812.08373>.
- [39] K. LEE AND K. CARLBERG, *Deep conservation: A latent dynamics model for exact satisfaction of physical conservation laws*, 2019, <https://arxiv.org/abs/1909.09754>.
- [40] M. LIANG AND X. HU, *Recurrent convolutional neural network for object recognition*, in The IEEE Conference on Computer Vision and Pattern Recognition (CVPR), June 2015.
- [41] R. MEAKIN, *Moving body overset grid methods for complete aircraft tiltrotor simulations*, <https://doi.org/10.2514/6.1993-3350>, <https://arc.aiaa.org/doi/abs/10.2514/6.1993-3350>, <https://arxiv.org/abs/https://arc.aiaa.org/doi/pdf/10.2514/6.1993-3350>.
- [42] V. MEHRMANN AND T. STYKEL, *Balanced truncation model reduction for large-scale systems in descriptor form*, in Dimension Reduction of Large-Scale Systems, P. Benner, D. C. Sorensen, and V. Mehrmann, eds., Berlin, Heidelberg, 2005, Springer Berlin Heidelberg, pp. 83–115.
- [43] R. MITTAL, H. DONG, M. BOZKURTAS, F. NAJJAR, A. VARGAS, AND A. [VON LOEBBECKE], *A versatile sharp interface immersed boundary method for incompressible flows with complex boundaries*, Journal of Computational Physics, 227 (2008), pp. 4825 – 4852, <https://doi.org/https://doi.org/10.1016/j.jcp.2008.01.028>, <http://www.sciencedirect.com/science/article/pii/S0021999108000235>.
- [44] F. MONTI, D. BOSCAINI, J. MASCI, E. RODOLA, J. SVOBODA, AND M. M. BRONSTEIN, *Geometric deep learning on graphs and manifolds using mixture model cnns*, in The IEEE Conference on Computer Vision and Pattern Recognition (CVPR), July 2017.
- [45] J. MORTON, F. D. WITHERDEN, AND M. J. KOCHENDERFER, *Parameter-conditioned sequential generative modeling of fluid flows*, 2019, <https://arxiv.org/abs/1912.06752>.
- [46] T. MURATA, K. FUKAMI, AND K. FUKAGATA, *Nonlinear mode decomposition with convolutional neural networks for fluid dynamics*, (2019).
- [47] K. NAKAHASHI, F. TOGASHI, AND D. SHAROV, *Intergrid-boundary definition method for overset unstructured grid approach*, AIAA Journal, 38 (2000), pp. 2077–2084, <https://doi.org/10.2514/2.869>, <https://doi.org/10.2514/2.869>, <https://arxiv.org/abs/https://doi.org/10.2514/2.869>.
- [48] N. OMATA AND S. SHIRAYAMA, *A novel method of low-dimensional representation for temporal behavior of flow fields using deep autoencoder*, AIP Advances, 9 (2019), p. 015006, <https://doi.org/10.1063/1.5067313>.
- [49] J. PARK, D. HWANG, K. KIM, S. KANG, Y. KIM, AND J. LEE, *Computed tomography super-resolution using deep convolutional neural network*, Physics in medicine and biology, 63 (2018), <https://doi.org/10.1088/1361-6560/aacdd4>.
- [50] C. S. PESKIN, *The immersed boundary method*, Acta Numerica, 11 (2002), p. 479517, <https://doi.org/10.1017/S0962492902000077>.
- [51] Y. PU, Z. GAN, R. HENAO, X. YUAN, C. LI, A. STEVENS, AND L. CARIN, *Variational autoencoder for deep learning of images, labels and captions*, in Advances in Neural Information Processing Systems 29, D. D. Lee, M. Sugiyama, U. V. Luxburg, I. Guyon, and R. Garnett, eds., Curran Associates, Inc., 2016, pp. 2352–2360, <http://papers.nips.cc/paper/6528-variational-autoencoder-for-deep-learning-of-images-labels-and-captions.pdf>.
- [52] Q. QIU, X. CHENG, R. CALDERBANK, AND G. SAPIRO, *Dcfnet: Deep neural network with decomposed convolutional filters*, (2018), <https://arxiv.org/abs/1802.04145>.
- [53] M. RASTEGARI, V. ORDONEZ, J. REDMON, AND A. FARHADI, *Xnor-net: Imagenet classification using binary convolutional neural networks*, in Computer Vision – ECCV 2016, B. Leibe, J. Matas, N. Sebe, and M. Welling, eds., Cham, 2016, Springer International Publishing, pp. 525–542.
- [54] P. RASTI, T. UIBOUPIN, S. ESCALERA, AND G. ANBARJAFARI, *Convolutional neural network super resolution for face recognition in surveillance monitoring*, in Articulated Motion and Deformable Objects, F. J. Perales and J. Kittler, eds., Cham, 2016, Springer International Publishing, pp. 175–184.
- [55] T. N. SAINATH, A. MOHAMED, B. KINGSBURY, AND B. RAMABHADRAN, *Deep convolutional neural networks for lcsr*, in 2013 IEEE International Conference on Acoustics, Speech and Signal Processing, May 2013, pp. 8614–8618, <https://doi.org/10.1109/ICASSP.2013.6639347>.
- [56] A. SEVERYN AND A. MOSCHITTI, *Twitter sentiment analysis with deep convolutional neural networks*, in Proceedings of the 38th International ACM SIGIR Conference on Research and Development in Information Retrieval, SIGIR 15, New York, NY, USA, 2015, Association for Computing Machinery, p. 959962, <https://doi.org/10.1145/2766462.2767830>, <https://doi.org/10.1145/2766462.2767830>.
- [57] R. SHANG, J. HE, J. WANG, K. XU, L. JIAO, AND R. STOLKIN, *Dense connection and depthwise*

- separable convolution based cnn for polarimetric sar image classification*, Knowledge-Based Systems, (2020), p. 105542, <https://doi.org/https://doi.org/10.1016/j.knosys.2020.105542>, <http://www.sciencedirect.com/science/article/pii/S0950705120300411>.
- [58] S. E. SHERER AND J. N. SCOTT, *High-order compact finite-difference methods on general overset grids*, Journal of Computational Physics, 210 (2005), pp. 459 – 496, <https://doi.org/https://doi.org/10.1016/j.jcp.2005.04.017>, <http://www.sciencedirect.com/science/article/pii/S0021999105002366>.
 - [59] D. I. SHUMAN, S. K. NARANG, P. FROSSARD, A. ORTEGA, AND P. VANDERGHEYNST, *The emerging field of signal processing on graphs: Extending high-dimensional data analysis to networks and other irregular domains*, IEEE Signal Processing Magazine, 30 (2013), p. 8398, <https://doi.org/10.1109/msp.2012.2235192>, <http://dx.doi.org/10.1109/MSP.2012.2235192>.
 - [60] K. SIMONYAN AND A. ZISSERMAN, *Very deep convolutional networks for large-scale image recognition*, 2014, <https://arxiv.org/abs/1409.1556>.
 - [61] R. STEWART AND S. ERMON, *Label-free supervision of neural networks with physics and domain knowledge*, CoRR, abs/1609.05566 (2016), <http://arxiv.org/abs/1609.05566>, <https://arxiv.org/abs/1609.05566>.
 - [62] C. M. STROFER, J.-L. WU, H. XIAO, AND E. PATERSON, *Data-driven, physics-based feature extraction from fluid flow fields using convolutional neural networks*, Communications in Computational Physics, 25 (2019), <https://doi.org/10.4208/cicp.oa-2018-0035>, <http://dx.doi.org/10.4208/cicp.OA-2018-0035>.
 - [63] C. SZEGEDY, W. LIU, Y. JIA, P. SERMANET, S. REED, D. ANGUELOV, D. ERHAN, V. VANHOUCHE, AND A. RABINOVICH, *Going deeper with convolutions*, in The IEEE Conference on Computer Vision and Pattern Recognition (CVPR), June 2015.
 - [64] Y. WANG, V. KIM, M. BRONSTEIN, AND J. SOLOMON, *Learning geometric operators on meshes*, Representation Learning on Graphs and Manifolds 2019 (ICLR workshop), (2019), <http://par.nsf.gov/biblio/10124350>.
 - [65] J. WILLCOX, K. PERAIRE, *Balanced model reduction via the proper orthogonal decomposition*, AIAA journal, (2002).
 - [66] L. WU, P. SUN, R. HONG, Y. FU, X. WANG, AND M. WANG, *Socialgen: An efficient graph convolutional network based model for social recommendation*, (2018), <https://arxiv.org/abs/1811.02815>.
 - [67] Z. WU, S. PAN, F. CHEN, G. LONG, C. ZHANG, AND P. S. YU, *A comprehensive survey on graph neural networks*, ArXiv, abs/1901.00596 (2019).
 - [68] J. YAMANAKA, S. KUWASHIMA, AND T. KURITA, *Fast and accurate image super resolution by deep cnn with skip connection and network in network*, in Neural Information Processing, D. Liu, S. Xie, Y. Li, D. Zhao, and E.-S. M. El-Alfy, eds., Cham, 2017, Springer International Publishing, pp. 217–225.
 - [69] Y. ZHANG, W.-J. SUNG, AND D. MAVRIS, *Application of convolutional neural network to predict airfoil lift coefficient*, 2017, <https://arxiv.org/abs/1712.10082>.
 - [70] J. ZHOU, G. CUI, Z. ZHANG, C. YANG, Z. LIU, AND M. SUN, *Graph neural networks: A review of methods and applications*, ArXiv, abs/1812.08434 (2018).
 - [71] Y. ZHU, N. ZABARAS, P.-S. KOUTSOURELAKIS, AND P. PERDIKARIS, *Physics-constrained deep learning for high-dimensional surrogate modeling and uncertainty quantification without labeled data*, Journal of Computational Physics, 394 (2019), pp. 56 – 81, <https://doi.org/https://doi.org/10.1016/j.jcp.2019.05.024>, <http://www.sciencedirect.com/science/article/pii/S0021999119303559>.